Probabilistic solving of *NP*-hard problems with bistable nonlinear optical networks

O. Kyriienko,[1,2,*] H. Sigurdsson,[3,4] and T. C. H. Liew[5,†]

[1]*NORDITA, KTH Royal Institute of Technology and Stockholm University, Roslagstullsbacken 23, SE-106 91 Stockholm, Sweden*

[2]*ITMO University, Saint Petersburg 197101, Russia*

[3]*Science Institute, University of Iceland, Dunhagi-3, IS-107 Reykjavik, Iceland*

[4]*School of Physics and Astronomy, University of Southampton, Southampton, SO17 1BJ, United Kingdom*

[5]*Division of Physics and Applied Physics, School of Physical and Mathematical Sciences, Nanyang Technological University, 21 Nanyang Link, Singapore 637371*

(Received 30 July 2018; revised manuscript received 23 April 2019; published 9 May 2019)

We study theoretically a lattice of locally bistable driven-dissipative nonlinear cavities. The system is found to resemble the classical Ising model and enables its effective simulation. First, we benchmark the performance of driven-dissipative nonlinear cavities for spin-glass problems, and study the scaling of the ground-state-energy deviation and success probability as a function of system size. Next, we show how an effective bias field can be included in an optical model and use it for probabilistic solving of optimization problems. As particular examples we consider *NP*-hard problems embedded in the Ising model, namely graph partitioning and the knapsack problem. Finally, we confirm that locally bistable polariton networks act as classical optimizers and can potentially provide an improvement within the exponential complexity class.

DOI: 10.1103/PhysRevB.99.195301

I. INTRODUCTION

Solving complex optimization problems is highly demanded in various fields of science and information technologies, ranging from economics [1] and finances [2] to biology and physics [3–5]. While certain problems can be solved deterministically in polynomial time and belong to class *P*, many optimization problems do not have a deterministic solution. Namely, these correspond to tasks in which the number of operations to obtain the true optimum scales exponentially, and the solution should be searched for probabilistically, thus falling into the nondeterministic polynomial (*NP*) complexity class. Methods include simulated annealing [6], Monte Carlo sampling [7], ant colony optimization [8], and genetic protocols [9], which represent improvement on brute force (greedy) algorithms. Some examples of *NP* problems are satisfiability, graph partitioning, and Hamiltonian-cycle problems (e.g., traveling salesman), among others [10]. They include *NP*-hard problems, which correspond to a search for the exact value of the optimal solution.

As *NP*-hard problems are ubiquitous in nature and their efficient solving strategies represent a major milestone in many areas, the problem has attracted much attention in computational science. One of the possible approaches was suggested in the field of quantum computing, where a quantum adiabatic algorithm searches for the ground state of an associated spin-glass-type Hamiltonian [11,12], which can be mapped to the solution of *NP*-complete problems [10,13]. The strategy also serves as a goal for large-scale quantum annealers built by DWave, Inc. [14], though operating in the open-system regime. However, thus far there is no significant evidence to suggest that there is an efficient (i.e., polynomial) quantum algorithm to solve *NP* tasks. To date, only constant speedup has been demonstrated [15]. This poses the question of whether alternative strategies using classical analog simulating devices can provide similar advantages. Recently, one of these devices—a degenerate optical parametric network—has attracted attention as a possible Ising model solver [16–19], and has shown scalability potential. Other considered options include pure [20] and hybrid photonic [21] quantum simulators.

A new emerging platform for classical simulation of effective spin models is the nonlinear system of exciton-polariton lattices [22–31]. Recently, several experiments reported the generation of real-space lattices of polaritonic wells, where each node corresponds to a coherent nonequilibrium condensate of polaritons [32,33]. Coupling was realized through the delocalized photonic component, and the exciton-exciton interaction provides nonlinearity. So far classical simulators for XY-type models have been considered [27,34,35], as well as spin chains [36]. Another way to arrange for nonlinear optical lattices is to host polaritons in photonic crystal structures, where both III-V semiconductor platforms [37,38] and two-dimensional materials [39] can be used.

In this paper we provide a general method to encode classical spin in the nonlinear optical system, and show its ability to find probabilistically the ground-state configuration for the effective Ising model. This is based on the mapping of high- or low-intensity optical states into a binary information [40]. The approach is inherently nonlinear, and is largely different from previously demonstrated phase-encoded Ising [18,19] and XY [27,34,41,42] simulators, both in driven-dissipative and coherent circuit settings [43]. We propose a feedback scheme that provides all-to-all coupling, and find that the suggested

*Corresponding author: kyriienko@ukr.net

†Corresponding author: timothyliew@ntu.edu.sg

 ©2019 American Physical Society

encoding allows us to tackle concrete optimization problems without extra overhead required by mapping from other models with sparse connectivity or bias-free systems [44]. This for instance can lead to huge improvements for system size, as an all-to-all-connected Ising model with $O(100)$ spins would require up to $O(10^6)$ auxiliary spins to be simulated with a 2D nearest neighbor connected graph [44].

We consider actual optimization problems and show that native Ising encoding is beneficial for small-scale optimizers. As an example, we apply bistable polaritonic networks to the *NP*-hard graph-partitioning problem, where Ising-type interaction is encoded into polaritonic intermode tunneling. Then, we introduce bias in the system and apply it to the knapsack problem, widely used in economics [45,46]. Finally, we discuss possible implementation using existing technology.

II. MODEL

Classical spin models with bistable states. To begin, we consider a system of spatially separated but interconnected nonlinear optical resonators. This can be represented by the coupled micropillars with an active medium inside, where nonlinearity is provided by the presence of matter quasiparticles (e.g., excitons) [25] or quantum emitters (defects, quantum dots) [47,48]. Despite the implementation differences, these setups correspond to the general class of driven-dissipative nonlinear lattices, and are described by the nonlinear Schrödinger equation for open systems (see Ref. [32] for an extensive review). This corresponds to the evolution equations in which each cavity (optical mode) is described by a complex field amplitude ψ_n. The system reads

$$i\hbar\frac{\partial\psi_n}{\partial t} = \left[-\Delta_n(t) - i\frac{\gamma_n}{2} + \alpha|\psi_n|^2\right]\psi_n + F_n(t) + \sum_m J_{nm}\psi_m. \tag{1}$$

F_n represents the amplitude of a coherent driving field acting on the mode n. We work in the frame oscillating at the frequency of this driving field, which we assume to be the same for all resonators. Δ_n represents the detuning between the driving frequency and the resonant frequency of the mode n. We allow for both F_n and Δ_n to be slowly varied over time. The dissipation in the system is represented by the term $-i\gamma_n/2$, where γ_n corresponds to the dissipation rate at each mode. In the following, we consider decay to be homogeneous such that $\gamma_n \equiv \gamma$. α corresponds to the strength of a repulsive (self-defocusing) Kerr nonlinearity. The term J_{nm} allows for coherent coupling between different modes, and in general enables all-to-all connectivity. While we identify exciton-polaritons in micropillar cavities as a potential implementation of the presented model, this also applies to a range of other nonlinear driven-dissipative bosonic systems (e.g., photonic crystals, superconducting circuits, and driven-dissipative superfluids [49]). Specifically, we target the situation of coherent excitation Josephson coupling between the modes [50,51]. However, we expect that similar results could be obtained with dissipative coupling mechanisms (i.e., imaginary J_{nm}) [27].

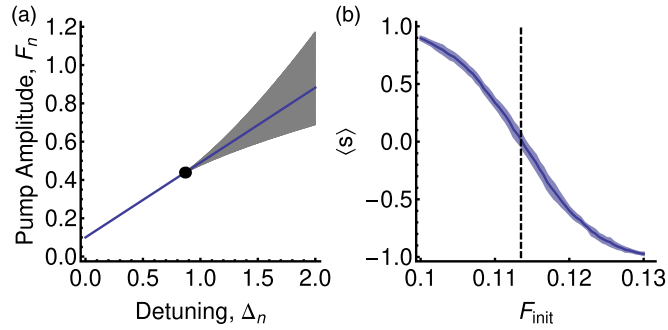

FIG. 1. (a) Bifurcation diagram of a single nonlinear driven-dissipative system, described by Eq. (2). In the shaded region the system is bistable, while in the unshaded region it is monostable. The solid point marks the bifurcation point and the solid line a possible ramping of system parameters. (b) Dependence of the average effective spin population on the initial pump amplitude after crossing the bifurcation point, with $\Delta_n(t)$ and $F_n(t)$ increasing linearly as stated in the text. The vertical line marks the value at which the effective spin population is zero on average, corresponding to $F^0_{\text{init}} = 0.1135$, and the noise level is set to $\theta_0 = 0.4$. The shading around the curve in (b) indicates the statistical error.

To perform the numerical analysis, it is convenient to use dimensionless parameters for Eq. (1), which reads

$$i\frac{\partial\widetilde{\psi}_n}{\partial\widetilde{t}} = \left[-\widetilde{\Delta}_n(t) - \frac{i}{2} + |\widetilde{\psi}_n|^2\right]\widetilde{\psi}_n + \widetilde{F}_n(t) + \sum_m \widetilde{J}_{nm}\widetilde{\psi}_m. \tag{2}$$

For this we rescale time in the units of inverse decay, $\widetilde{t} = t\gamma$, energy is measured in units of $\hbar\gamma$ [$\widetilde{\Delta} = \Delta/(\hbar\gamma)$ and $\widetilde{J} = J/(\hbar\gamma)$], the nonlinear interaction strength is absorbed in the definition of the field amplitude, $\widetilde{\psi}_n = \psi_n\sqrt{\alpha/(\hbar\gamma)}$, and the pump amplitude is rescaled as $\widetilde{F} = F\alpha^{1/2}/(\hbar\gamma)^{3/2}$. Thus, by changing the laser intensity one can tune the effective amount of nonlinearity in the system. For brevity, in the following we remove the tildes and consider the dimensionless parameters throughout the rest of the paper.

A. Single-mode case

It is instructive to first consider a single isolated mode. Taking Δ_n and F_n to be constant and setting the time derivative in Eq. (1) to zero yields a cubic equation for the stationary-state intensity $|\psi_n|^2$, namely, $[(\Delta - |\psi_n|^2)^2 + 1/4]|\psi_n|^2 = |F_n|^2$. In general the cubic equation yields three solutions; whether or not they are real depends on parameters. The possibilities are illustrated in Fig. 1(a), which shows two types of behavior: in the unshaded region there is only one real stationary solution corresponding to monostable behavior, while in the shaded region all three solutions are real. In this latter case two of the solutions are stable and have different intensities, while the third solution is unstable. Consequently the system is considered bistable, with both low- and high-intensity states possible under the same conditions. The effect of bistability in nonlinear optical systems is well known, and we refer to textbooks for the didactic description [52,53]. Another system that can show pronounced bistable behavior is a system of exciton-polaritons [54]. In Fig. 1(a) we can identify a

bifurcation point separating the bistable and monostable regions, at the critical pump amplitude $F_c = 3^{-3/4}$ and critical detuning $\Delta_c = \sqrt{3}/2$.

The solid line in Fig. 1(a) represents a possible slow (adiabatic) ramping of the parameters $F_n(t)$ and $\Delta_n(t)$ according to $\Delta_n(t) = \Delta_c t/\tau$ and $F_n(t) = F_{n,\text{init}} + (F_c - F_{n,\text{init}})t/\tau$. Here, $F_{n,\text{init}}$ defines the initial value of F_n and τ is the time at which the bifurcation point is reached. Following this path of parameters, a bifurcation point is expected [40], where the system must choose one of the two possible bistable states to lie in thereafter. The interplay of local bistability and Josephson coupling has been studied previously in Kerr nonlinear lattices, showing lattice solitons [55–57], various collective phases [58,59], interaction-induced hopping [50], phase-controlled bistability [60], cellular automata [61], and topological behavior [62].

To model the stochastic choice of the system at the bifurcation point we add a noise term θ_n to the right-hand side of Eq. (1), where $\langle \theta_n^* \theta_m \rangle = 2\theta_0^2 \delta_{n,m} dt$ and $\langle \theta_n \theta_m \rangle = 0$. The magnitude of such a term can be controlled experimentally and it can cause jumps between bistable states [63]. The probability of a jump is high near the bifurcation point and decreases as one moves farther and farther beyond the bifurcation point. The choice of bistable state after passing the bifurcation point also depends on the angle of the line along which the parameters are ramped up in the F_n-Δ_n plane. We define an effective classical spin as $s = \pm 1$ depending on whether the system chooses the higher- or lower-intensity state when in the bistable zone. Figure 1(b) shows how the average of this effective spin, obtained by calculating over different realizations of the stochastic noise, varies with F_{init}. For a value of $F_{\text{init}}^0 = 0.1135$, for which the line in Fig. 1(a) passes between the lower and upper boundaries of the bifurcation zone, we find an equal chance to form high- or low-intensity states, corresponding to $\langle s \rangle = 0$.

B. Two-mode case

Next, we consider the case of two coupled modes and provide a motivation for encoding of an Ising model into bistable states for the modes. While we only claim empirical evidence for a heuristic rather than exact global minimizer, there is an intuition underlying the operation of our system. For two coupled modes, the evolution of the system is described by the equations (neglecting the noise terms)

$$i\frac{d\psi_1}{dt} = (-\Delta - i/2 + |\psi_1|^2)\psi_1 + F + J\psi_2, \tag{3}$$

$$i\frac{d\psi_2}{dt} = (-\Delta - i/2 + |\psi_2|^2)\psi_2 + F + J\psi_1. \tag{4}$$

Without coupling (in the absence of J) and above the bifurcation point the possible solutions, (ψ_1, ψ_2), are (ψ_L, ψ_L), (ψ_L, ψ_U), (ψ_U, ψ_L), and (ψ_U, ψ_U), where ψ_L and ψ_U are the lower- and upper-intensity single-mode stationary solutions. We recall that when the system is in a stationary solution it evolves with a real energy. This is set to zero here as we are working in the frame rotating with the pump frequency. Considering first the state (ψ_L, ψ_L), we are interested in how its energy changes in the presence of coupling J. Setting $\psi_{1,2} = \psi_L \exp(-i\omega_{1,2}t)$, that is, allowing the energy of the stationary state to be changed and become complex (such that it is no longer stationary),

$$i\frac{d\psi_1}{dt} = \omega_1\psi_L = J\psi_L, \tag{5}$$

$$i\frac{d\psi_2}{dt} = \omega_2\psi_L = J\psi_L. \tag{6}$$

Here, we have made the crude approximation on the right-hand side, assuming that the influence of one mode on another is approximately given by taking the influencing mode as being in the single-mode solution. While a very rough approximation, it illustrates the principle: ω_1 and ω_2 do not change much from the single-mode stationary values when both modes are in the low-intensity state. The same occurs when considering both modes in the upper-intensity state, that is, $(\psi_1, \psi_2) = (\psi_U, \psi_U)$. However, considering the case $(\psi_1, \psi_2) = (\psi_L, \psi_U)$, we obtain

$$i\frac{d\psi_1}{dt} = \omega_1\psi_L = J\psi_U, \tag{7}$$

$$i\frac{d\psi_2}{dt} = \omega_2\psi_U = J\psi_L. \tag{8}$$

Here we find that $\omega_1 = J\psi_U/\psi_L$ and $\omega_2 = J\psi_L/\psi_U$. Above the bifurcation point, it is straightforward to find from the analytic solutions that ψ_U/ψ_L has a negative imaginary part, while ψ_L/ψ_U has a positive imaginary part. Thus, the effect of $J > 0$ on (ψ_L, ψ_U) is to make ψ_1 drop in intensity and ψ_2 grow in intensity. This suggests that the state (ψ_L, ψ_U), that is, an antiferromagnetic state, is more stable due to the coupling J. The argument applies in the same way to the state opposite the antiferromagnetic state, (ψ_U, ψ_L). We can also note that if $J < 0$, the antiferromagnetic state will instead be less stable as the signs of ω_1 and ω_2 will be inverted. Thus, when the system passes the bifurcation point and is fluctuating in the presence of noise, the picture is that because the antiferromagnetic state (for $J > 0$) is more stable it is more likely to be chosen by the system. However, to verify this picture we need to consider the basins of attraction of the system in phase space [64]. While it is an educated guess that a deeper basin of attraction is also larger in phase space, we are not aware of any law to be certain before actually calculating it.

Figure 2(a) shows the phase diagram of the single-mode system. There are two fixed points, corresponding to the low-intensity (small dot) and high-intensity (large dot) bistable states. The solid curve denotes the separatrix, corresponding to the boundary between basins of attraction between the two fixed points. Figure 2(b) shows how the phase diagram of mode ψ_1 is modified by coupling to a second mode ψ_2, assuming that the second mode ψ_2 is in the lower-intensity state (treated with the single-mode approximation). Remarkably, not only does the basin of attraction for the upper-intensity state grow, as expected from the crude analysis presented above, but it fills the whole phase space as the lower-intensity state has become unstable [therefore no separatrix for this case can be plotted and only comparison with case Fig. 2(a) is shown by the blue solid line]. We have also observed the opposite behavior, namely the upper intensity becoming unstable, when $J < 0$ (not shown in the plot). Figure 2(c) shows the phase diagram of mode ψ_1 when coupled to a

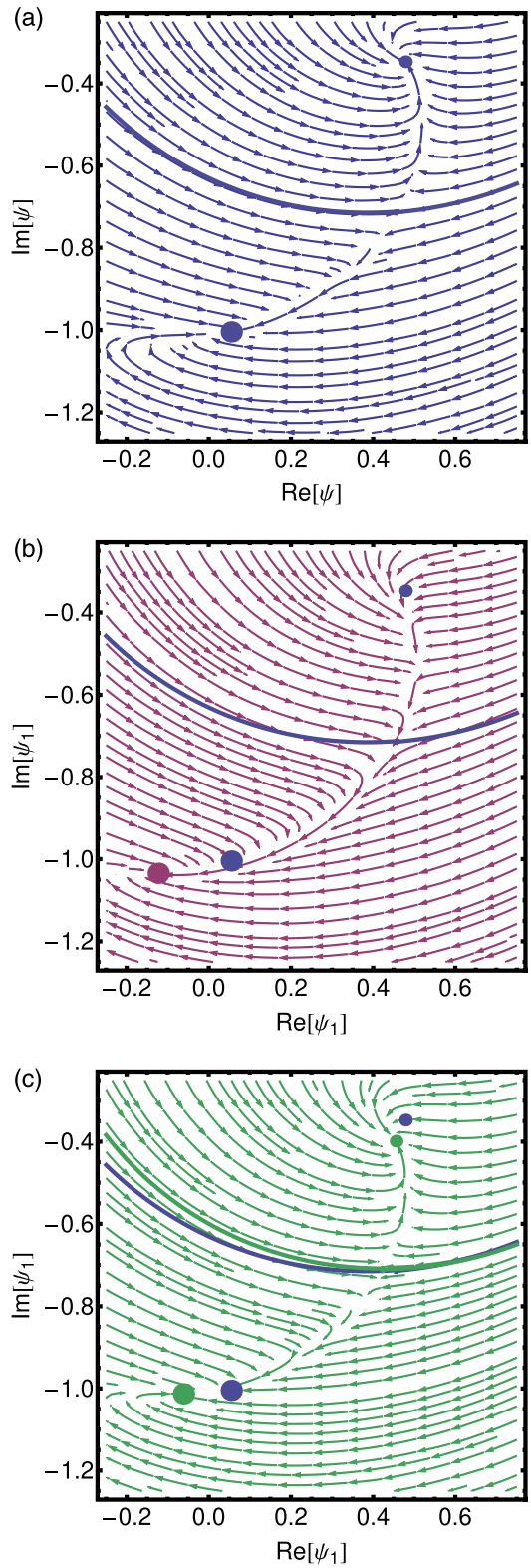

FIG. 2. Phase diagrams for (a) a single-mode system (blue), (b) a mode ψ_1 coupled to a mode ψ_2 in the lower intensity state (purple), and (c) a mode ψ_1 coupled to a mode ψ_2 in the upper intensity state (green). Parameters were taken the same as in Fig. 1(b), with $dF_{\text{init}} = 0$ and $t = 1.2\tau$. $J > 0$ case is considered, with $J = 0.04$. The large and small spots represent fixed points of high and low intensity, respectively. The solid curves mark separatrices, blue for the single-mode system and green for the mode coupled to a mode in the upper intensity state.

second mode in the upper-intensity state (again treated with the single-mode approximation). In this case the low-intensity state has been stabilized. Although the separatrix is little changed from the single-mode case, the shown behavior allows the antiferromagnetic state to be stable in our system.

C. Multimode case

Finally, building on the single- and two-mode examples, we consider the multimode case of coupled nonlinear cavities. We note that while the phase diagrams in Fig. 2 describe well the mechanism at play for a two-coupled-mode system, generalization to larger systems is not trivial. Recent work using a functional-integral approach was successful in showing that Eq. (2) exhibits an emergent equilibrium, where the system tends to the state of an effective Ising Hamiltonian [40]. Here we consider a heuristic approach and will consider empirical testing of application of the studied system to different problems, using multiple trajectories to sample the multidimensional phase space.

To address complex optimization problems, we take an all-to-all-type coupling J_{nm}. In principle, this could be realized with a feedback approach [65] in which the optical output of all modes is extracted and fed back into the system after some manipulation. For this we propose several schemes that can allow for coupling between cavities. First, the feedback can be realized using an optical matrix multiplier composed of a pair of lenses and a spatial light modulator [66–68] (see Appendix A for the details of the scheme). Namely, using the emitted light that goes through a Fourier lens, the localized modes in the real space of the microcavity can be mapped to the reciprocal space of a plane behind the lens. Next, using the spatial light modulator different Fourier components are mixed, reflected, and fed back into the cavity array. We note that a feedback approach was exploited successfully for coherent Ising machines, leading to large connectivity [18]. Second, an alternative scheme to realize a highly connected graph can be arranged with a bus-coupled mechanism. It relies on the effective coupling through a detuned bus mode, such that effective all-to-all coupling of different magnitudes can be realized, suitable for the graph-partitioning problem (see Appendix B for the detailed description).

III. RESULTS

A typical example of the system dynamics for a randomly chosen coupling matrix J_{nm} is shown in Fig. 3(a) for $N = 10$. The coherent drive amplitude $F_n(t)$ and detuning $\Delta_n(t)$ are chosen the same for all modes and ramped slowly through the bifurcation point [following the solid line in Fig. 1(a)]. The overall scale of the couplings is taken such that their root-mean-squared value $\langle J_{nm}\rangle$ is kept small ($\lesssim 0.1$), and that it can be considered as a perturbation to the single-mode dynamics. After crossing the bifurcation point, all modes adopt either a high or low intensity, close to the exact adiabatic solutions for the single-mode case. Remarkably, although our N-mode system is multistable, for the particular noise realization used in Fig. 3(a), we find empirically that the system attains the state minimizing the effective Ising Hamiltonian with arbitrary connectivity, $H_{\text{eff}} = \sum_{n,m} J_{nm} s_n s_m$, corresponding to a spin-glass system. An underlying intuition for this behavior

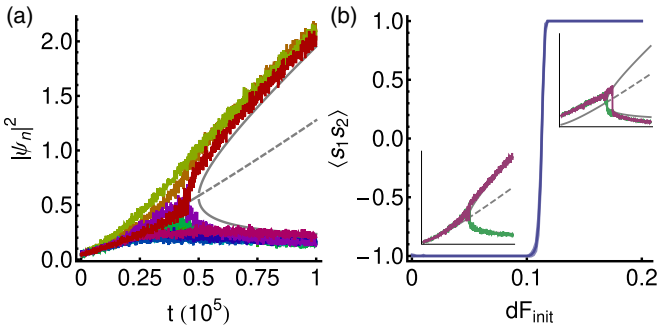

FIG. 3. (a) Colored curves show the evolution of $|\psi_n|^2$ for a ten-mode system slowly ramped through the bifurcation point. The solid gray curves show the stable stationary solutions followed by the single-mode system in the adiabatic limit; the dashed gray curve shows an unstable branch associated with the bistable region. J_{nm} was chosen as a real symmetric matrix with Gaussian-distributed values of root-mean-square size 0.04. Other parameters are the same as in Fig. 1, using the unbiased value $F^0_{\rm init} = 0.1135$ corresponding to the vertical dashed line in Fig. 1(b). (b) Dependence of the effective spin correlation, $\langle s_1 s_2 \rangle$, for two antiferromagnetically coupled modes ($J_{12} = 0.04$) on the difference in the initial pump amplitude from the unbiased value. The insets show the time dependence, using the same axes as in (a).

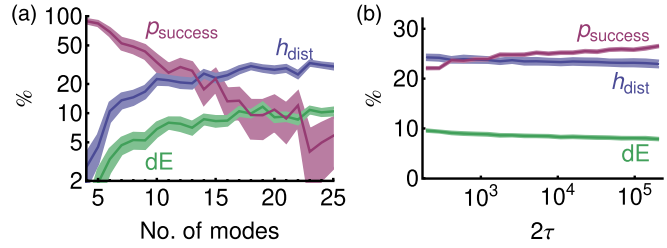

FIG. 4. (a) Variation of the average Hamming distance $h_{\rm dist}$, energy difference from the ground state dE, and success probability $p_{\rm success}$ (all in logarithmic scale) with the number of modes in the system. Here the value of $\langle J \rangle$ was taken as the optimum for each number of modes. Parameters were taken the same as in Figs. 1 and 3(a), with $2\tau = 10^4$. The shading around the curves indicates the standard error. (b) Variation of the average Hamming distance, normalized energy difference from the ground state, and success probability as a function of the system integration time 2τ. The shading around the curves indicates the standard error. Parameters: $F^0_{\rm init} = 0.1135$, $\langle J \rangle = 0.04$, $\theta_0 = 0.4$.

can be based on the behavior of the basins of attraction of the system described in the previous section, where we find that two coupled modes with $J_{nm} > 0$ are more likely to form in an antiferromagnetic state. The obtained state is sensitive to $F_{\rm n,init}$, as expected from its influence on the single-mode behavior [Fig. 1(b)]. Figure 3(b) shows that antiferromagnetically coupled modes may be forced into a ferromagnetic state under sufficient adjustment of $F_{\rm init} = F^0_{\rm init} + dF_{\rm init}$. Considering the $N = 10$ system with different noise realizations, the optimal solution appeared in over 30% of tries, which largely exceeds the probability of random guesses for the problem.

A. Spin-glass benchmarking

To characterize the polariton optimizer, we repeated our calculations with different randomly generated coupling matrices J_{nm}. The performance was benchmarked by comparison to the ideal ground state of $H_{\rm eff}$ using several metrics. The Hamming distance $h_{\rm dist} = (1/N)\sum_n^N (1 - s_n s_n^{(g)})/2$ is a measure of how far in configurational space the obtained s_n and ideal ground states $s_n^{(g)}$ are. We also defined the energy difference of the approximate solution E and the ground state as $dE = (E - E_g)/(E_{\rm max} - E_g)$, where the normalization factor allows us to consider various instances on equal footing. Finally, the success probability $p_{\rm success}$ was defined as the probability of having *exactly* the ground-state energy.

Considering, for simplicity, the zero-bias case (setting $F_{\rm init} = F^0_{\rm init}$ as for the single-mode system), Fig. 4(a) shows the variation of the different performance characteristics as the system size is increased. For each system size there is an optimum of the overall scale of the coupling $\langle J \rangle$, which was chosen by scanning over $\langle J \rangle$. While the success probability is less than unity, it is finite, and the ability of an optical system to reach a state promptly makes it feasible to rerun the simulator several times.

The total calculation time taken for the simulator to obtain the correct result after several trials is then inversely proportional to the success probability and scales exponentially with the system size, as is expected for a nonpolynomial problem. Even when a state different from the ground state is found, the Hamming distance and energy difference suggest that it is still a reasonable approximation of the ground state.

We also studied the success probability as a function of ramping time for $F_n(t)$ and $\Delta_n(t)$. We found that the performance of the considered polariton simulator depends weakly on the rate at which the parameters are ramped through the bifurcation point. Taking a system of 10 modes, with randomly chosen couplings and no bias, we show in Fig. 4(b) the variation with the system integration time. Here, τ represents the time at which the bifurcation point is reached and 2τ is the total integration time at which the system state is measured. The results suggest overall but weak improvement for slower operation times. However, in practice it may be viable to take smaller τ, while performing more repetitions. Given that the polariton lifetime can be around a picosecond, and ultrafast switching of bistable states is well established [69–71], we conservatively predict device operation times of nanoseconds with little loss of success probability.

B. Graph partitioning

We now show an Ising-type embedding of the *NP*-hard graph-partitioning problem and solve it simulating the bistability-based polaritonic optimizer. Given the graph $G = (V, E)$ with vertices $V = \{v_j\}_{j=1}^{N_v}$ and the set of edges, $E = \{e_k\}_{k=1}^{N_e}$, the task is to find the partitioning into two groups of equal numbers of vertices (assume N_v being even) such that the number of edges connecting the groups is minimized [10]. It is also related to the max-cut problem, albeit without assigning distances (i.e., different weights) to the edges. Such a task can be used to speed up classical high-performance computing providing the routes for efficient parallelization.

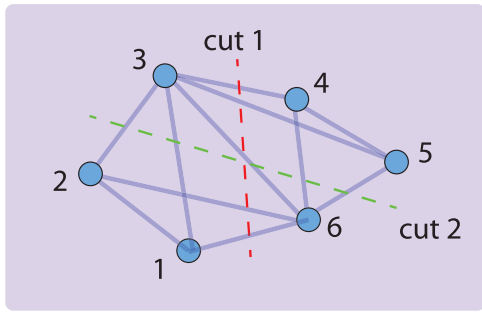

FIG. 5. Sketch of the graph-partitioning problem, aiming to find two separated sets of modes. For the chosen connection net, the ground-state solutions are represented by two possible cuts (red and green lines).

The problem can be formulated as the minimization of an all-to-all-connected Ising Hamiltonian,

$$H = J \sum_{(k,l)\in E} (1 - s_k s_l)/2 + J\beta \sum_{(i,j)\in V}^{N_v} s_i s_j, \tag{9}$$

where J and β are real positive parameters. The spin variables $s_i = \pm 1$ label the nodes of two groups to be minimally coupled. Here, the first term assures that each connection between the two groups of spins introduces an energy penalty, and for $J > 0$ the number of edges will be minimized. The second term represents a constraint and ensures that the total spin is zero, thus giving equal partitioning for large β (see Ref. [10] for the introductory description of *NP*-hard problem embeddings). Rearranging terms in the Hamiltonian (9) shows that to solve the graph-partitioning problem one should find the ground state of the Ising Hamiltonian. Due to the problem encoding we observe that Eq. (9) contains interaction terms with coupling of two magnitudes, βJ and $(\beta - 1/2)J$. This, for instance, can be encoded in the real-space coupled polariton nodes through the common bus (see Appendix B).

As a particular test, we can choose the small system of size of $N_v = 6$ vertices, where

$$E = \{(1,2),(2,3),(3,4),(4,5),(5,6),\\ (1,3),(3,5),(4,6),(3,6),(2,6),(1,6)\} \tag{10}$$

corresponds to a dense connection grid, where the ratio for the number of connections at each node to the total number of sites becomes comparable to unity. The problem's topology is depicted in Fig. 5. The optimal partitioning then corresponds to two degenerate energy configurations (in addition to spin degeneracy), being $[\{1,2,3\},\{4,5,6\}]$ and $[\{1,2,6\},\{3,4,5\}]$ (see corresponding cuts 1 and 2 in Fig. 5), which are encoded in the $\{-1,-1,-1,1,1,1\}$ and $\{-1,-1,1,1,1,-1\}$ spin configurations (or their bit-flipped partners).

Figure 6 shows that while the overall scale of J and the value of β should be carefully chosen, the system can solve the graph-partitioning problem. We also consider the scaling of the graph-partitioning problem. For this, we average the success probability and energy deviation over randomly selected graphs. Each graph is taken to have a number of connections equal to one-half the total number of possible

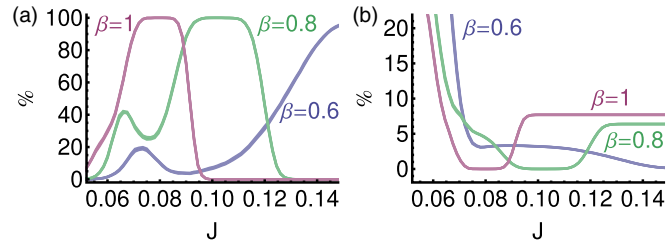

FIG. 6. Variation of the success probability p_{success} (a) and energy difference from the ground state dE (b) for solving the graph-partitioning problem with J for a graph with $N = 6$ and different values of β (marked on the plots). Other parameters were taken the same as in Figs. 1 and 3(a), with $2\tau = 10^4$. The standard error is within the line thickness.

connections for each given system size (similar results can be obtained for different connection fractions). The results are shown in Fig. 7, suggesting that while the overall success probability (within the adopted definition) drops, the average Hamming distance and energy deviation persist.

C. Knapsack problem

As a further example of an *NP*-hard problem potentially solved by the nonlinear optical network, we consider the knapsack problem. Having the list of N objects of fixed weight (w_i) and cost (c_i), we want to fill a knapsack maximizing its cost, given that the maximal total weight is limited to $W_{\max}$. Here, i is an item index running from 1 to N, weights correspond to integer-valued numbers, and we introduce a binary variable s_i, which is equal to 1 when an object is inside the box and 0 otherwise (see Fig. 8). The total weight and total value then read $W = \sum_{i=1}^{N} w_i s_i$ and $C = \sum_{i=1}^{N} c_i s_i$, respectively. We further introduce auxiliary binary variables a_j, where the index j runs from 1 to $W_{\max}$, being the maximal weight. The classical Hamiltonian corresponding to the problem then reads

$$H = \alpha \left(1 - \sum_{j=1}^{W_{\max}} a_j\right)^2 + \alpha \left(\sum_{j=1}^{W_{\max}} j a_j - \sum_{i=1}^{N} w_i s_i\right)^2 - \beta \sum_{i=1}^{N} c_i s_i, \tag{11}$$

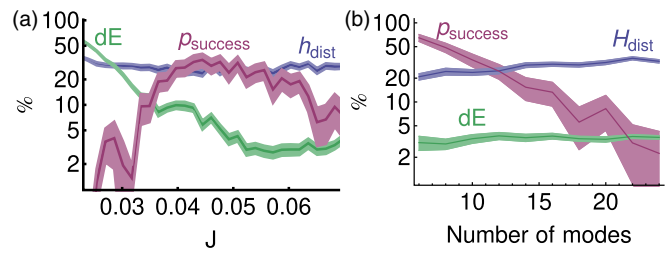

FIG. 7. Variation of the average Hamming distance h_{dist}, energy difference from the ground state dE, and success probability p_{success} (all in logarithmic scale) for partitioning random graphs for a system of size $N = 10$ (a) and random graphs of different sizes taking in each case the optimum J (b). Other parameters were taken the same as in Fig. 6, with $\beta = 1$.

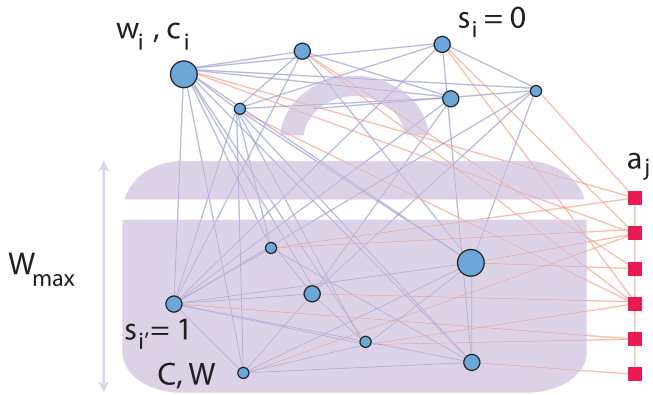

FIG. 8. Sketch of the knapsack problem. Different items of weight w_i and cost c_i can be placed in the suitcase (assign binary variable $s = 1$), or left outside ($s = 0$). The maximal weight of the suitcase is bounded by $W_{\max}$. The solution can be obtained by searching for minimal energy configuration for combined item (s_i) and auxiliary (a_i) spins, combined into an all-to-all-connected Ising network.

where α and β are parameters for the simulation, chosen such that the global minimum of (11) corresponds to the solution. The Hamiltonian (11) can be rewritten as the standard all-to-all-connected Ising model with bias terms h_n as (where we now take $s_n = \pm 1$)

$$H := -\sum_{n<m}^{N+W_{\max}} J_{nm} s_n s_m - \sum_{n=1}^{N+W_{\max}} h_n s_n, \tag{12}$$

where J_{nm} denotes the Ising coupling matrix, formed by weights, and h_n is an effective magnetic field formed by the combination of cost and weight. The parameters are inferred from the original encoding given in Eq. (11).

The knapsack problem represents a ubiquitous problem in the field of finances and portfolio optimization [45,72], resource allocation problems, cargo-loading problems, and others. Its solution, for instance, provides the answer on how one can choose the best portfolio basket given the limited resources.

As a test we choose an instance of the knapsack problem in its bounded version. In particular, we consider the example with 3 coins of weight 1 and value 5 (coin *a*), 2 coins of weight 2 and value 10 (coin *b*), and 1 coin of weight 3 and value 25 (coin *c*). The maximal weight is fixed to $W_{\max} = 9$. Using a brute-force algorithm, which considers all possible item (i.e., spin) configurations, the solution is 2 *a* coins, 2 *b* coins, and 1 *c* coin. In the classical spin language these are three degenerate configurations, $\{s\} = [\{-1, 1, 1, 1, 1, 1\}, \{1, -1, 1, 1, 1, 1\}, \{1, 1, -1, 1, 1, 1\}]$.

Next, we simulate the dynamics of a corresponding polariton network in order to solve the same problem. For this, recalling that the average effective spin population depends on F_{init} [as shown in Fig. 1(b)], we identify the difference of F_{init} from the value favoring equal spin populations in the single-mode system as an effective biasing parameter h_n. Using the effective bias, the outlined knapsack problem with 15 spins in total is modeled by time-evolving Eq. (1) with the corresponding matrix J_{nm} and the appropriate vector of biases

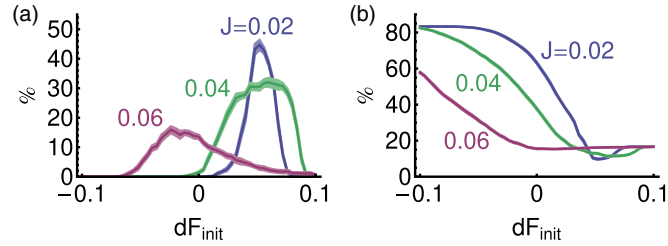

FIG. 9. Success probability (a) and Hamming distance (b) for solving the fifteen-mode knapsack problem with a polariton simulator. The plots show the variation with the overall scale of dF_{init}, for different values of J (marked on the plots). Parameters were taken the same as in Fig. 3, although considering the effective spin Hamiltonian with bias terms representing a specific instance of the knapsack problem. The shading around the curves indicates the standard error and $2\tau = 10^4$.

dF_{init}. The probability of successfully reaching the ground state of the effective Hamiltonian is shown in Fig. 9 as a function of the overall scale of dF_n, where we find a success probability ~50% for optimally chosen parameters. While for the problem with unknown solution the choosing of optimal dF_{init} is not straightforward, it can be assessed using a sweep over a range of values followed by sampling, and searching for the optimal configuration in each case. Later the choice of dF_{init} can be refined. In Appendix C we consider the variation of the system performance for randomly chosen knapsack problems.

IV. CONCLUSIONS

We have considered nonlinear, near-resonantly excited, optical-cavity lattices as coherent driven-dissipative machines that are capable of solving Ising-type optimization problems. We presented an encoding scheme for binary information based on bistable behavior of each lattice site, which naturally appears for photons due to the Kerr-type interaction. Two possible schemes for experimental implementation of an all-to-all-connected real-space polariton network were proposed, and were exploited to solve graph partitioning and the knapsack problem. While the results do not suggest improved scaling with system size, showing approximately exponential reduction of the probability of getting the correct ground state, the devices can speed up calculation because of fast operation (a few nanoseconds for $N = 20$ modes with $\sim 10^6$ configurations) and use of now-well-established fabrication techniques of photonic systems. As mechanisms of resonantly driven multistability are established experimentally [70,73,74], generalization to such models seems within reach, together with consideration of nonresonantly driven mechanisms of bistability [75,76]. The described results can be applied to various nonlinear optical systems, including nonlinear plasmonics [77], silicon photonics [78], and vibron-polaritons [79].

ACKNOWLEDGMENTS

We thank N. G. Berloff for useful comments on the manuscript. H.S. acknowledges support by the research fund of the University of Iceland, the Icelandic Research Fund,

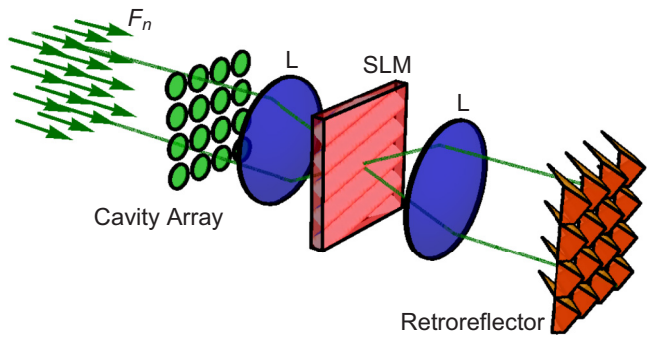

FIG. 10. Example scheme of all-to-all coupling using a spatial light modulator (SLM). The cavity array, corresponding to an array of micropillar cavities, photonic crystal cavities, or other set of nonlinear modes, is coherently excited by the driving field, F_n. The transmitted light from the cavity array is passed through a Fourier lens (L), which maps the spatially separated modes to Fourier space. If the SLM contains a component at the difference wave vector of the modes, it can allow their coupling in Fourier space via diffraction. The light is retroreflected and returned to the real space after passing back through the original Fourier lens so as to feed back into the cavity array.

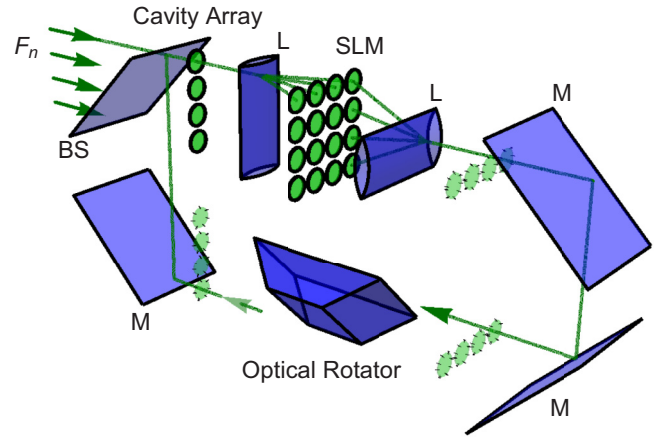

FIG. 11. Example scheme of feedback loop providing all-to-all coupling. The transmitted light from the cavity array is fed through an optical matrix multiplier, composed of a combination of lenses (L) and an SLM. The light is then reflected by a series of mirrors (M) and an optical rotator (e.g., Dove prism) before being overlapped with the original driving field, with the aid of a beam splitter (BS), and being fed back into the cavity array.

Grant No. 163082-051, and from UK's Engineering and Physical Sciences Research Council (Grant EP/M025330/1 on Hybrid Polaritonics). The work was partly supported by the Government of the Russian Federation through the ITMO Fellowship and Professorship Program. T.C.H.L. was supported by the Ministry of Education (Singapore), Grant No. 2017-T2-1-001.

APPENDIX A: FEEDBACK SCHEME

Here, we present the details of a setup that can potentially enable high connectivity for polaritonic graphs. We consider a planar polaritonic system, for example where a cavity is formed by distributed Bragg reflectors and the active medium corresponds to a stack of quantum wells, hosting excitonic quasiparticles. The lattice of localized modes can be created by an optical potential, and each mode is fully separated in space and can be driven resonantly. Assuming that the substrate on which the cavity array is grown is transparent, light is emitted through the back surface. When this emitted light passes through a Fourier lens, the localized modes in the real space of the microcavity are mapped to the reciprocal space of a plane behind the lens. There one can place a spatial light modulator (SLM), represented by material with spatially modulated refractive index (Fig. 10). Thus, in this plane we expect a coupling of the different modes according to the weights given by the Fourier components of the effective potential (refractive index variation) set by the spatial light modulator. Placing another mirror or retroreflector behind the spatial light modulator ensures that the light is reflected and fed back into the cavity array. Using the Fourier lens, the modes in the reciprocal space of the spatial modulator $\psi_{\mathbf{k}}$ are then mapped back to the real-space modes of the active medium, $\psi_{\mathbf{x}}$.

As an alternative, the traditional optical matrix multiplier method could be employed (Fig. 11). In this case the cavities are arranged into a 1D array. A lens maps their output into an array, which is focused and modulated on a spatial light modulator. The transmitted signal is mapped by a second lens into a 1D array that is returned to the original cavity array via a feedback loop.

As compared to the scheme in Fig. 10, this alternative allows one to operate with a lower-resolution SLM (e.g., a shadow mask could also be used), while the overall system size is larger since the cavity array is stretched out into a 1D rather than 2D array.

The described schemes correspond to a specific form of optical input-output network (ION) with coherent feedback control. The idea of ION originated from the cascade formalism from input-output theory [80] and dates back to early work by Wiseman and Milburn [81]. Mathematically, it can be treated within the SLH framework, which provides the formal approach to treat optical systems with feedback [82]. A detailed review on the subject can be found in Ref. [83]. Given access to passive-mode-mixing devices and feedback, networks of arbitrary connectivity can be arranged in coherent fashion. Here, we start with providing the generic approach and show a simple example, leaving the question of a full multimode network for a separate specialized study.

The central object of the SLH theory corresponds to the system operator G described as a triple $G = (S, L, H)$ that contains operators of the input-output scattering (S), the coupling between the system and input-output ports (L), and the system Hamiltonian (H). The equation of motion for the unitary evolution operator of the system $U(t)$ can be generally written as

$$dU(t) = \left\{-\left(iH + \tfrac{1}{2}L^{\dagger}L\right)dt + LdB_{in}^{\dagger}(t) \right. \tag{A1}$$

$$\left. - L^{\dagger}SdB_{in}(t)\right\}U(t), \tag{A2}$$

where the evolution is written in Ito form and $dB_{in}(t)$ is an increment of the input field vector [83]. Then, given the set of modes $\{\hat{a}_j\}_{j=1}^{N}$, the Heisenberg equations of motion for any

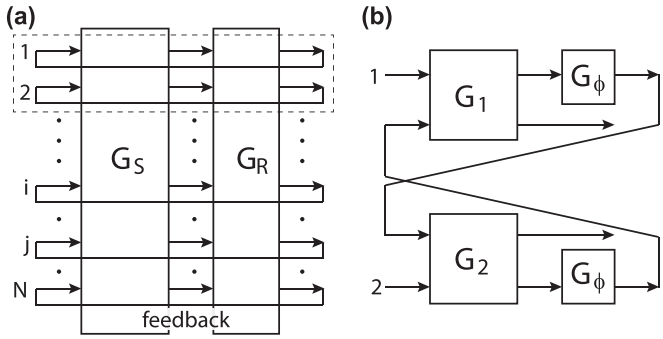

FIG. 12. (a) General N-mode SLH scheme with the feedback loop through a retroreflector. (b) The two-mode system with feedback that allows for effective coupling between the modes through optical loops and phase shifters.

mode $\hat{a}_j$ can be written as

$$\hat{a}_j(t) = U^\dagger(t)\hat{a}_j U(t), \tag{A3}$$

where $U(t)$ is obtained from Eq. (A1) by integration. The behavior of the composite system is then defined by the lumped triple $G_F = (S_F, L_F, H_F)$. In schematic fashion the SLH equivalent of the retroreflector scheme is shown in Fig. 12(a). Here, the first block corresponding to the SLH triple G_S describes the system, the second block denotes the retroreflector triple G_R, followed by the coherent feedback loop. To provide a concrete and intuitive example, we consider the two-mode case with phase shifts and feedback, which models the simplest retroreflector. The scheme is presented in Fig. 12(b). Here $G_1 = (I_2, [L_1, L_{1'}]^T, H_1)$ and $G_2 = (I_2, [L_2, L_{2'}]^T, H_2)$ correspond to mode 1 and 2 triples. In our case Hamiltonians correspond to $\Delta_{1,2}\hat{a}^\dagger_{1,2}\hat{a}_{1,2}$ mode energies; $L_{1,1'}$ and $L_{2,2'}$ describe the input-output port couplings and for equal coupling rates $\kappa_{1,2}$ read $L_{1,1'} = \sqrt{\kappa_1}\hat{a}_1$, $L_{2,2'} = \sqrt{\kappa_2}\hat{a}_2$. The scattering matrix is represented by the identity I_2 acting in the Hilbert space of the two modes. The phase shifter is described by $G_\phi = (e^{i\phi}, 0, 0)$. Finally, the output of the circuit can be written using the SLH formalism, leading to

$$G_F = (S_F, L_F, H_F) = G_1 \boxplus G_\phi \boxplus G_\phi \boxplus G_2, \tag{A4}$$

where the $\boxplus$ operation denotes the concatenation product for the circuits. After the feedback reduction and elimination of the internal connections, the reduced circuit can be written as triple $G_{\rm red} = (S_{\rm red}, L_{\rm red}, H_{\rm red})$, with

$$S_{\rm red} = e^{i\phi} I_2, \tag{A5}$$

$$L_{\rm red} = \begin{pmatrix} e^{i\phi}L_1 + L_2 \\ e^{i\phi}L_{2'} + L_{1'} \end{pmatrix}, \tag{A6}$$

$$H_{\rm red} = H_1 + H_2 - \frac{i}{2}(e^{i\phi}L_1 L_2^\dagger - e^{-i\phi}L_1^\dagger L_2 + e^{i\phi}L_{1'}^\dagger L_{2'} - e^{-i\phi}L_{1'}L_{2'}^\dagger). \tag{A7}$$

An important consequence of the presence of the feedback loop along with the shift is a generation of the coupling between modes. This can be seen in the effective Hamiltonian $H_{\rm red} \propto i(\hat{a}_1^\dagger\hat{a}_2 - \hat{a}_2^\dagger\hat{a}_1)$, once we use the explicit form for the input-output coupling operators. The magnitude of the coupling is then controlled by the parameters of the retroreflector, which can mix the signals with different weights.

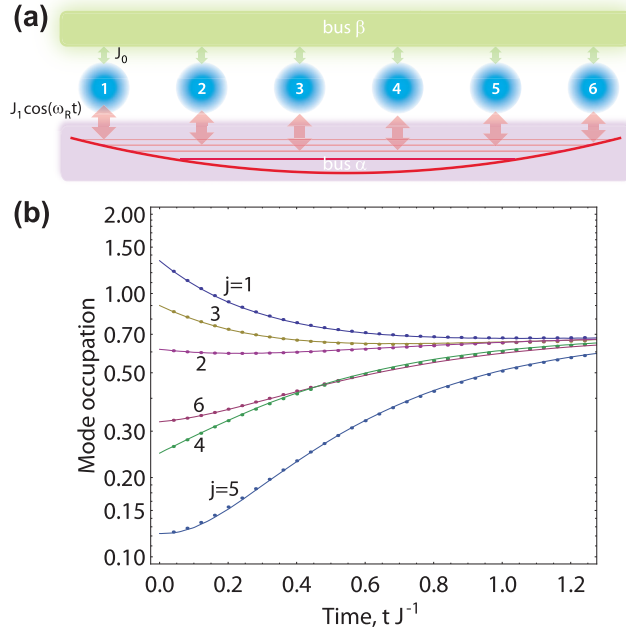

FIG. 13. (a) Bus-coupled polaritonic boxes. The all-to-all coupling is realized though a detuned common bus (top channel). Additionally, the edge coupling for the particular graph is realized with a multimode bus (bus α, bottom) with multiplexed coupling. (b) The proof-of-principle calculation of a six-mode system coupled through three bus modes. The plot shows the intensity for each mode ($j = 1, \ldots, 6$) for the full time-dependent calculation (curves) and effective eliminated version (dots), which coincide.

APPENDIX B: BUS-COUPLED SCHEME

We consider a chain of unconnected polariton wells, where the wave function in each box is described by the mean field ψ_n. We take the situation in which there is no direct coupling between different polariton boxes, but there is a channel that runs alongside the chain that represents a coherent polariton bus, similar to a quantum-connecting bus used for microwave circuits [84]. In particular we consider two types of buses, being geometrically suitable for the graph-partitioning problem [bus α and bus β in Fig. 13(a)].

The top channel is described by macroscopic wave function χ_0, and is detuned to frequency f_0. This would allow us to effectively realize homogeneous all-to-all coupling, which is for instance required by the second term in Hamiltonian (9) of the main text. The bottom channel contains a set of modes, described by mean field χ_m ($m \geqslant 1$) and bare frequency f_m. If we further imagine that the potential between the bottom channel and each polariton box is modulated in time, then we can write the equations of motion:

$$\frac{\partial\psi_n}{\partial t} = (-i\Delta_n - \gamma_n/2)\psi_n + F_n - iJ_0\chi_0 - i\sum_m J_{nm}\cos(\omega_m t)\chi_m - |\psi_n|^2\psi_n, \tag{B1}$$

$$\frac{\partial \chi_m}{\partial t} = -i\omega_m \chi_m - i\sum_n J_{nm}\cos(\omega_m t)\psi_n - \chi_m, \tag{B2}$$

$$\frac{\partial \chi_0}{\partial t} = -i\omega_0 \chi_0 - iJ_0 \sum_n \psi_n - \chi_0, \tag{B3}$$

where F_n is a coherent pump amplitude for the nth mode with detuning Δ_n and decay γ_n. Here J_{nm} characterizes the coupling strength between the localized mode ψ_n and channel mode χ_m, which is modulated at frequency ω_m. J_0 is the homogeneous coupling to the β bus.

We account for nonlinear losses in the equation for the localized modes, which may undergo condensation (the amount of nonlinear losses has been scaled to unity through the definition of ψ and χ). We also account for losses of the channel modes, by an amount scaled to unity through the timescale. We consider the bus modes to be nondriven. Now, let $\chi_m = \chi'_m e^{-i\omega_m t}$, such that

$$\frac{\partial \chi'_m}{\partial t} = -i\sum_n J_{nm}\cos(\omega_m t)e^{i\omega_m t}\psi_n - \chi'_m$$

$$\approx \frac{-i}{2}\sum_n J_{nm}\psi_n - \chi'_m, \tag{B4}$$

where we neglect fast-oscillating components. Solving the last equation for the stationary state and assuming fast dynamics for the bus, we can rewrite the system using effective couplings for the modes. Similarly, the stationary solution for χ_0 (static bus) gives

$$\chi_0 = -\frac{J_0}{\omega_0 - i}\sum_n \psi_n. \tag{B5}$$

Substituting the stationary solutions into Eq. (B1) gives the effective couplings. This ultimately allows us to arrange J and $J\beta$ terms for the partitioning problem.

To test the validity of the used approximation, we perform the dynamical simulation of an $N = 6$ mode system with three dynamical buses, which are detuned by 25, 10, and -15 energy units (measured by the channel's decay rate), and are coupled through $J_{nm} = 1$. Other parameters are $F_n = \gamma_n = 1$, $J_0 = 0$, and we take random initial conditions. The results are shown in Fig. 13(b), and reveal that the mode intensities can be successfully described by the effective theory, where time-dependent coupling is converted into selective intermode interaction.

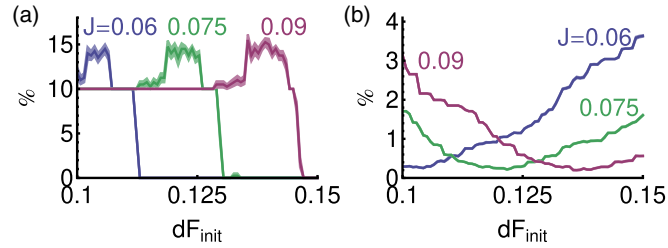

FIG. 14. Success probability (a) and energy difference from the ground state (b) for solving random fifteen-mode knapsack problems with a polariton simulator. The problem size is fixed, such that as in the main text six coins are considered, although here they have random weights and costs. The knapsack problem again seeks to maximize the cost, while not exceeding a fixed maximum weight. Other parameters were taken the same as in Fig. 9.

APPENDIX C: RANDOM KNAPSACK PROBLEMS

As shown in the main text, the success probability of solving the knapsack depends on the chosen system parameters, in particular F_{init} and J. In principle the optimum parameters can depend on the specific instance of the knapsack problem. To avoid optimization of each problem from scratch, in Fig. 14 we consider the system performance averaged over randomly generated knapsack problems of a fixed size.

It can be seen that general optimum parameters can be identified even when averaging over randomly generated problems. Although the success probability is less than for optimizing a specific problem, it is notable that the energy difference from the ground state is small. This result shows that when one is interested in solving many different knapsack problems, for example an economics problem that varies daily, good parameters can be set from the beginning and reused.

[1] J.-P. Bouchaud, J. Stat. Phys. **151**, 567 (2013).
[2] S. N. Durlauf, Proc. Natl. Acad. Sci. USA **96**, 10582 (1999).
[3] J. D. Bryngelson and P. G. Wolynes, Proc. Natl. Acad. Sci. USA **84**, 7524 (1987).
[4] N. A. Pierce and E. Winfree, Pro. Eng. Design Select. **15**, 779 (2002).
[5] H. Nishimori, *Statistical Physics of Spin Glasses and Information Processing: An Introduction* (Oxford University Press, Oxford, 2008).
[6] K. A. Dowsland and J. M. Thompson, Simulated annealing, in *Handbook of Natural Computing*, edited by G. Rozenberg, T. Bäck, and J. N. Kok (Springer, Berlin, 2012).
[7] R. H. Swendsen and J.-S. Wang, Phys. Rev. Lett. **57**, 2607 (1986).
[8] M. Dorigo, V. Maniezzo, and A. Colorni, IEEE Trans. Syst. Man Cyber. Part B (Cyber.) **26**, 29 (1996).
[9] J. McCall, J. Comput. Appl. Math. **184**, 205 (2005).
[10] A. Lucas, Front. Phys. **2**, 5 (2014).
[11] E. Farhi, J. Goldstone, S. Gutmann, J. Lapan, A. Lundgren, and D. Preda, Science **292**, 472 (2001).
[12] T. Kadowaki and H. Nishimori, Phys. Rev. E **58**, 5355 (1998).
[13] F. Barahona, J. Phys. A: Math. Gen. **15**, 3241 (1982).
[14] N. G. Dickson *et al.*, Nat. Commun. **4**, 1903 (2013).
[15] V. S. Denchev, S. Boixo, S. V. Isakov, N. Ding, R. Babbush, V. Smelyanskiy, J. Martinis, and H. Neven, Phys. Rev. X **6**, 031015 (2016).
[16] A. Marandi, Z. Wang, K. Takata, R. L. Byer, and Y. Yamamoto, Nat. Photonics **8**, 937 (2014).

[17] T. Inagaki, Y. Haribara, K. Igarashi, T. Sonobe, S. Tamate, T. Honjo, A. Marandi, P. L. McMahon, T. Umeki, K. Enbutsu, O. Tadanaga, H. Takenouchi, K. Aihara, K.-i. Kawarabayashi, K. Inoue, S. Utsunomiya, and H. Takesue, Science **354**, 603 (2016).

[18] P. L. McMahon, A. Marandi, Y. Haribara, R. Hamerly, C. Langrock, S. Tamate, T. Inagaki, H. Takesue, S. Utsunomiya, K. Aihara, R. L. Byer, M. M. Fejer, H. Mabuchi, and Y. Yamamoto, Science **354**, 614 (2016).

[19] W. R. Clements, J. J. Renema, Y. H. Wen, H. M. Chrzanowski, W. S. Kolthammer, and I. A. Walmsley, Phys. Rev. A **96**, 043850 (2017).

[20] A. Aspuru-Guzik and P. Walther, Nat. Phys. **8**, 285 (2012).

[21] D. G. Angelakis, editor, *Quantum Simulations with Photons and Polaritons*, Quantum Science and Technology (Springer International Publishing, Cham, Switzerland, 2017).

[22] C. W. Lai, N. Y. Kim, S. Utsunomiya, G. Roumpos, H. Deng, M. D. Fraser, T. Byrnes, P. Recher, N. Kumada, T. Fujisawa, and Y. Yamamoto, Nature (London) **450**, 529 (2007).

[23] N. Y. Kim, K. Kusudo, C. Wu, N. Masumoto, A. Löffler, S. Höfling, N. Kumada, L. Worschech, A. Forchel, and Y. Yamamoto, Nat. Phys. **7**, 681 (2011).

[24] G. Tosi, G. Christmann, N. G. Berloff, P. Tsotsis, T. Gao, Z. Hatzopoulos, P. G. Savvidis, and J. J. Baumberg, Nat. Commun. **3**, 1243 (2012).

[25] T. Jacqmin, I. Carusotto, I. Sagnes, M. Abbarchi, D. D. Solnyshkov, G. Malpuech, E. Galopin, A. Lemaître, J. Bloch, and A. Amo, Phys. Rev. Lett. **112**, 116402 (2014).

[26] K. Winkler, J. Fischer, A. Schade, M. Amthor, R. Dall, J. Geler, M. Emmerling, E. A. Ostrovskaya, M. Kamp, C. Schneider, and S. Höfling, New J. Phys. **17**, 023001 (2015).

[27] N. G. Berloff, K. Kalinin, M. Silva, W. Langbein, and P. G. Lagoudakis, Nat. Mater. **16**, 1120 (2016).

[28] S. Klembt, T. H. Harder, O. A. Egorov, K. Winkler, H. Suchomel, J. Beierlein, M. Emmerling, C. Schneider, and S. Höfling, Appl. Phys. Lett. **111**, 231102 (2017).

[29] C. E. Whittaker, E. Cancellieri, P. M. Walker, D. R. Gulevich, H. Schomerus, D. Vaitiekus, B. Royall, D. M. Whittaker, E. Clarke, I. V. Iorsh, I. A. Shelykh, M. S. Skolnick, and D. N. Krizhanovskii, Phys. Rev. Lett. **120**, 097401 (2018).

[30] H. Ohadi, Y. del Valle-Inclan Redondo, A. J. Ramsay, Z. Hatzopoulos, T. C. H. Liew, P. R. Eastham, P. G. Savvidis, and J. J. Baumberg, Phys. Rev. B **97**, 195109 (2018).

[31] H. Suchomel, S. Klembt, T. H. Harder, M. Klaas, O. A. Egorov, K. Winkler, M. Emmerling, S. Hoefling, and C. Schneider, Phys. Rev. Lett. **121**, 257402 (2018).

[32] I. Carusotto and C. Ciuti, Rev. Mod. Phys. **85**, 299 (2013).

[33] T. Byrnes, N. Y. Kim, and Y. Yamamoto, Nat. Phys. **10**, 803 (2014).

[34] K. Kalinin, P. G. Lagoudakis, and N. G. Berloff, arXiv:1709.04683.

[35] K. P. Kalinin and N. G. Berloff, New J. Phys. **20**, 113023 (2018).

[36] H. Ohadi, A. J. Ramsay, H. Sigurdsson, Y. del Valle-Inclan Redondo, S. I. Tsintzos, Z. Hatzopoulos, T. C. H. Liew, I. A. Shelykh, Y. G. Rubo, P. G. Savvidis, and J. J. Baumberg, Phys. Rev. Lett. **119**, 067401 (2017).

[37] D. Bajoni, D. Gerace, M. Galli, J. Bloch, R. Braive, I. Sagnes, A. Miard, A. Lemaître, M. Patrini, and L. C. Andreani, Phys. Rev. B **80**, 201308(R) (2009).

[38] N. Y. Kim, K. Kusud, A. Löffler, S. Höfling, A. Forchel, and Y. Yamamoto, New J. Phys. **15**, 035032 (2013).

[39] Long Zhang, R. Gogna, W. Burg, E. Tutuc, and Hui Deng, Nat. Commun. **9**, 713 (2018).

[40] M. Foss-Feig, P. Niroula, J. T. Young, M. Hafezi, A. V. Gorshkov, R. M. Wilson, and M. F. Maghrebi, Phys. Rev. A **95**, 043826 (2017).

[41] K. P. Kalinin and N. G. Berloff, Phys. Rev. Lett. **121**, 235302 (2018).

[42] K. P. Kalinin and N. G. Berloff, Sci. Rep. **8**, 17791 (2018).

[43] H. Goto, Z. Lin, and Y. Nakamura, Sci. Rep. **8**, 7154 (2018).

[44] G. De las Cuevas and T. S. Cubitt, Science **351**, 1180 (2016).

[45] H. Kellerer, U. Pferschy, and D. Pisinger, *Knapsack Problems* (Springer-Verlag, Berlin, 2004).

[46] D. Deniz, A. Gershkov, and B. Moldovanu, Theoretical Economics **6**, 157 (2011).

[47] M. J. Hartmann, F. G. S. L. Brandão, and M. B. Plenio, Nat. Phys. **2**, 849 (2006).

[48] D. G. Angelakis, M. F. Santos, and S. Bose, Phys. Rev. A **76**, 031805(R) (2007).

[49] R. Labouvie, B. Santra, S. Heun, and H. Ott, Phys. Rev. Lett. **116**, 235302 (2016).

[50] S. R. K. Rodriguez, A. Amo, I. Sagnes, L. Le Gratiet, E. Galopin, A. Lemaître, and J. Bloch, Nat. Commun. **7**, 11887 (2016).

[51] A. F. Adiyatullin, M. D. Anderson, H. Flayac, M. T. Portella-Oberli, F. Jabeen, C. Ouellet-Plamandon, G. C. Sallen, and B. Deveaud, Nat. Commun. **8**, 1329 (2017).

[52] H. M. Gibbs, *Optical Bistability: Controlling Light with Light* (Academic Press, New York, 1985).

[53] A. E. Siegman, *Lasers* (University Science Books, Mill Valley, California, 1986).

[54] A. Baas, J. P. Karr, H. Eleuch, and E. Giacobino, Phys. Rev. A **69**, 023809 (2004).

[55] A. V. Yulin, A. R. Champneys, and D. V. Skryabin, Phys. Rev. A **78**, 011804(R) (2008).

[56] O. A. Egorov and F. Lederer, Opt. Lett. **38**, 1010 (2013).

[57] Y. V. Kartashov and D. V. Skryabin, Opt. Lett. **41**, 5043 (2016).

[58] I. Carusotto, D. Gerace, H. E. Tureci, S. De Liberato, C. Ciuti, and A. Imamoglu, Phys. Rev. Lett. **103**, 033601 (2009).

[59] A. Le Boité, G. Orso, and C. Ciuti, Phys. Rev. Lett. **110**, 233601 (2013).

[60] V. Goblot, H. S. Nguyen, I. Carusotto, E. Galopin, A. Lemaître, I. Sagnes, A. Amo, and J. Bloch, Phys. Rev. Lett. **117**, 217401 (2016).

[61] J. Li and T. C. H. Liew, Opt. Exp. **24**, 24930 (2016).

[62] Y. V. Kartashov and D. V. Skryabin, Phys. Rev. Lett. **119**, 253904 (2017).

[63] H. Abbaspour, S. Trebaol, F. Morier-Genoud, M. T. Portella-Oberli, and B. Deveaud, Phys. Rev. Lett. **113**, 057401 (2014).

[64] Z. Wang, A. Marandi, K. Wen, R. L. Byer, and Y. Yamamoto, Phys. Rev. A **88**, 063853 (2013).

[65] T. Byrnes, S. Koyama, K. Yan, and Y. Yamamoto, Sci. Rep. **3**, 2531 (2013).

[66] A. D. McAulay, *Optical Computer Architectures: The Application of Optical Concepts to Next Generation Computers* (Wiley-Interscience, New York, NY, 1991).

[67] M. A. Karim and A. A. S. Awwal, *Optical Computing: An Introduction* (John Wiley & Sons, New York, NY, 1992).

[68] J. W. Goodman, *Introduction to Fourier Optics* (W. H. Freeman, 1996).
[69] M. De Giorgi, D. Ballarini, E. Cancellieri, F. M. Marchetti, M. H. Szymanska, C. Tejedor, R. Cingolani, E. Giacobino, A. Bramati, G. Gigli, and D. Sanvitto, Phys. Rev. Lett. **109**, 266407 (2012).
[70] R. Cerna, Y. Léger, T. K. Paraïso, M. Wouters, F. Morier-Genoud, M. T. Portella-Oberli, and B. Deveaud, Nat. Commun. **4**, 2008 (2013).
[71] E. Cancellieri, A. Hayat, A. M. Steinberg, E. Giacobino, and A. Bramati, Phys. Rev. Lett. **112**, 053601 (2014).
[72] H. Morita, H. Ishii, and T. Nishida, Euro. J. Operat. Res. **40**, 329 (1989).
[73] T. K. Paraïso, M. Wouters, Y. Léger, F. Morier-Genoud, and B. Deveaud-Plédran, Nat. Mater. **9**, 655 (2010).
[74] G. Grosso, S. Trebaol, M. Wouters, F. Morier-Genoud, M. T. Portella-Oberli, and B. Deveaud, Phys. Rev. B **90**, 045307 (2014).
[75] M. Klaas, H. Sigurdsson, T. C. H. Liew, S. Klembt, M. Amthor, F. Hartmann, L. Worschech, C. Schneider, and S. Höfling, Phys. Rev. B **96**, 041301(R) (2017).
[76] L. Pickup, K. Kalinin, A. Askitopoulos, Z. Hatzopoulos, P. G. Savvidis, N. G. Berloff, and P. G. Lagoudakis, Phys. Rev. Lett. **120**, 225301 (2018).
[77] M. Kauranen and A. V. Zayats, Nat. Photonics **6**, 737 (2012).
[78] K. Vandoorne, P. Mechet, T. Van Vaerenbergh, M. Fiers, G. Morthier, D. Verstraeten, B. Schrauwen, J. Dambre, and P. Bienstman, Nat. Commun. **5**, 3541 (2014).
[79] A. V. Zasedatelev, A. V. Baranikov, D. Urbonas, F. Scafirimuto, U. Scherf, T. Stöferle, R. F. Mahrt, and P. G. Lagoudakis, Nat. Photonics (2019), doi: 10.1038/s41566-019-0392-8.
[80] M. J. Collett and C. W. Gardiner, Phys. Rev. A **30**, 1386 (1984).
[81] H. M. Wiseman and G. J. Milburn, Phys. Rev. A **49**, 4110 (1994).
[82] J. Gough, Phys. Rev. E **90**, 062109 (2014).
[83] J. Combes, J. Kerckhoff, and M. Sarovar, Adv. Phys.: X **2**, 784 (2017).
[84] C. Song, K. Xu, W. Liu, C.-p. Yang, S.-B. Zheng, H. Deng, Q. Xie, K. Huang, Q. Guo, L. Zhang, P. Zhang, D. Xu, D. Zheng, X. Zhu, H. Wang, Y.-A. Chen, C.-Y. Lu, S. Han, and J.-W. Pan, Phys. Rev. Lett. **119**, 180511 (2017).